Mechanism and Machine Theory 173 (2022) 104819

Contents lists available at ScienceDirect

Mechanism and Machine Theory

journal homepage: www.elsevier.com/locate/mechmt

Research paper

Experimental validation of a constant-force mechanism and analysis of its performance with a calibrated multibody model

Silvia Sánchez-Salinas [a], Alfonso García-Agúndez [b], Javier López-Martínez [a,*], Daniel García-Vallejo [b]

[a] CIMEDES Research Center (CeiA3), Department of Engineering, University of Almería, Spain
[b] Department of Mechanical Engineering and Manufacturing, Universidad de Sevilla, Spain

ARTICLE INFO

Keywords:
Constant-force mechanisms
Multibody model
Experimental validation

ABSTRACT

The potential applications of constant-force mechanisms (CFMs) have increased in recent years with the development of new designs. This paper focuses on the experimental evaluation and the mathematical modelling of a CFM. The mechanism is based on the use of cams, rollers and springs, which allows for a large stroke and user-adjustable force value. The evaluation and validation of the mechanism is carried out by performing a series of tests examining the constancy of the input force, and where the influence of friction forces and the manufacturing process on the performance of the mechanism is revealed. A multibody model of the constant-force mechanism is developed and calibrated with the help of the experimental results. This model is based on the assumption of rolling without sliding between the cam and the roller, what makes the multibody model to include velocity constraints. The calibration of the model pursues the development of a mathematical tool to study the performance of the mechanism in conditions that are different from those of the experiments presented. The CFM model is used to perform a sensitivity analysis of some important design parameters of the mechanism.

1. Introduction

Constant-force mechanisms (CFMs) are designed to achieve a constant force value on the input link for a certain prescribed range of displacement. These mechanisms are applied in several fields of engineering, where the design solution given in each case will depend on the intended use.

Constant-force mechanisms can be classified into two main groups according to the type of components that provide mobility to the mechanism [1]. A first group includes those mechanisms based on flexible links, the so-called compliant mechanisms [2–4], where the mobility of these mechanisms is provided by flexible elements and can be designed in one single piece. The flexible parts are usually designed with relatively complex geometries to achieve the characteristic of constant-force in a certain range of movement of the mechanism. The geometry of the flexible element can be obtained from optimization techniques [5–9] and from the pseudo-rigid body method [5,10–13]. Compliant CFMs can be designed for a one directional constant force [14,15] or for a constant torque [7,16]. Some CFMs proposals are based on the use of a positive stiffness element together with a negative stiffness element, so that when acting together the resulting force–displacement curve presents some region with null or almost null slope, i.e. nearly null stiffness [13,17–20]. One way to achieve negative stiffness is by using beam elements subjected to buckling, where

* Correspondence to: CIMEDES Research Center (CeiA3), Department of Engineering, University of Almería, 04120, Almería, Spain.
E-mail addresses: silvia.sanchez@ual.es (S. Sánchez-Salinas), agarciaagundez@us.es (A. García-Agúndez), javier.lopez@ual.es (J. López-Martínez), dgvallejo@us.es (D. García-Vallejo).

https://doi.org/10.1016/j.mechmachtheory.2022.104819
Received 2 December 2021; Received in revised form 2 February 2022; Accepted 3 March 2022
Available online 23 March 2022

the stiffness of the beam can be known from the Euler equation [21–23]. Compliant CFMs are of particular interest in applications that do not require large displacements, have the advantage of being simple and compact construction, and have no friction losses.

The second group of CFMs includes those that use springs together with a non-linear transmission. Compared to compliant CFMs, they have the advantage of being designed for larger displacements [15,24], although in most cases the influence of the friction must be taken into account in the design [14,24,25]. Some proposals are based on the use of rigid links together with springs arranged in a particular configuration [26–28], as is the case of the well known desk lamp holder, which compensates the weight of the lamp for a wide range of positions [29]. In other cases springs are used together with cams with a particular geometry. In some designs a non-circular cam rotates winding a cable around its surface, which lengthens a linear spring. By combining the linear spring characteristic with the variable radius cam, a constant torque can be achieved on the cam's axis of rotation [30,31]. Other designs use springs and rollers, where the springs are lengthened by rolling the rollers over a cam surface [14,15,24,32,33]. The particular geometry of the cam allows maintaining a constant force value on the input link of the mechanism. Some solutions allow the force value to be modified by presetting the initial spring tension [14] or by arranging several springs in parallel [24].

A generalization of the CFMs are mechanisms with user-defined stiffness. Instead of designing the mechanism for zero stiffness (constant force), the same design methods can be applied to obtain a non-linear spring with an specific stiffness curve [34,35]. Bidgoly et al. [36] derive the geometry of several cams to achieve constant torque, cubic, hyperbolic tangent and sinusoidal springs.

Constant-force mechanisms are undergoing considerable development in the field of robotics, where they are used as gravity-balancing mechanism [28], as safety systems against overloads [17], or in the manipulation of objects to limit the gripping force [8,19,37,38], thus avoiding the use of complex force control systems. CFMs have found new applications in fields such as surgery, with the design of grasping forceps to control the clamping force [10,39] or in cardiac ablation catheter [40]; in the development of 2-DOF grippers [41]; in assistive exoskeletons [42]; in end-effectors for polishing/deburring operations [43]; in microgripers for biological cell micromanipulation [44]; in body building machines, where they seek to eliminate the inertia forces present in weight-stack machines [45,46] or for their use in low-gravity environments [47]; in snap-fit connectors [48]; in automotive clutches [49] or in electrical contacts [50].

The multibody modelling of cam mechanisms is a problem that is definitively influenced by the contact modelling between the cam and the follower. Using multibody system dynamics theory, Cardona et al. [51] presented a methodology for the optimal design of the cams of motor engine valve trains including nonlinear geometrical, kinematical and dynamical constraints. Ouyang et al. [52] also utilized a dynamic multibody model of a cam-follower mechanism in the optimal design problem of the cam profile. The contact problem between circular and non-circular bodies, as that of the cam and the follower in general cam mechanisms, has been treated in detail by Xu [53], who proposed a general methodology for planar multibody systems which is applicable in case single and multi-point contact. Since cam profiles are often numerically represented, it is common to use interpolation to reconstruct the cam profile between data points. In this sense, the influence of interpolation errors in the kinematics and dynamics of cam mechanisms is studied by Borboni et al. [54]. Analyses of computational multibody models' results of cam mechanisms in comparison with experimental performance data can be found in the works of [55,56].

In the present work, a CFM based on a cam and springs is experimentally evaluated and mathematically modelled and studied. The CFM prototype evaluated here is based on one of the three conceptual designs of CFMs proposed in a previous work [24], and is intended for the future fabrication of a full-scale CFM for bodybuilding machines [45].

This paper is organized as follows: Section 2 includes, first, a brief description of the conceptual design of the CFM developed, the force equation condition for constant force and the numerical derivation for the cam profile; second, the description of the prototype developed; and third, the evaluation of the manufacturing errors in the fabricated cam. Section 3 contains a series of tests carried out to evaluate the performance of the mechanism and includes some simulations for comparison. Next, Section 4 deals with the formulation of the multibody model of the CFM and Section 5 discusses the influence of different parameters on the constant force characteristic. Lastly, Section 6 draws the main conclusions.

2. The constant-force mechanism

The CFM developed basically comprises a symmetric cam profile, two rollers, and a spring attached to both roller axes (Fig. 1). The pulling force is exerted on a cable (or a rod) aligned with the axis of symmetry of the mechanism, where this cable bifurcates into two braces that are connected to both roller axes respectively. As the cable moves vertically, the rollers move upward by rolling over the cam surface and the spring elongates by exerting a force opposing the movement. With this arrangement, a certain cam profile can be found that allows a constant force value to be maintained throughout the entire stroke of the mechanism.

Once the conceptual design of the CFM has been introduced, this section begins with a summary of the input force equation, the constant force condition, and the numerical integration required to obtain the roller centre trajectory (a more detailed description of this procedure can be found in our former work [24]). Subsequently, the CFM prototype is described. Finally, the manufacturing errors of the cam profile are measured and discussed.

2.1. Force equation and cam profile

Fig. 1 shows the forces acting on the right roller when the roller moves upward. Note that, due to the symmetry of the mechanism, both rollers move at the same time and the force diagrams are also the same for both rollers. From the equilibrium equations in

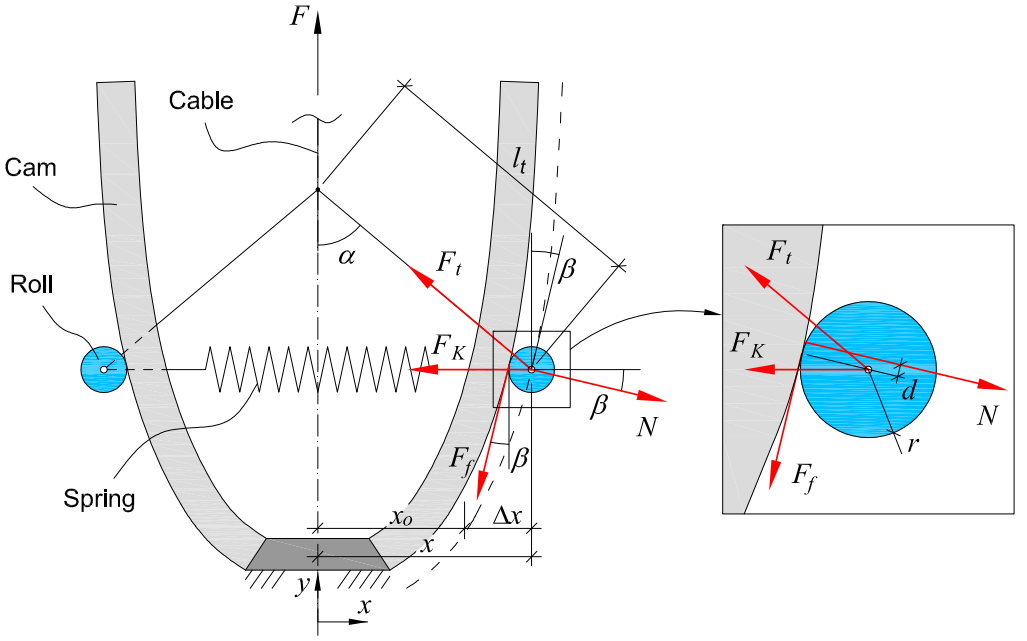

Fig. 1. Conceptual design of the CFM and forces diagram for the roller.

the horizontal and vertical directions, the moment equilibrium equation $F_f r = Nd$, and some basic relations, the input force can be written as [24]

$$F = \underbrace{4K\,\Delta x\left(\frac{1-\mu_r\tan\beta}{\tan\beta+\mu_r}-\tan\alpha\right)^{-1}}_{A}, \tag{1}$$

where the input force F results as a function of the spring stiffness coefficient K and its elongation Δx, the rolling friction μ_r, the slope of the curve β and the angle α of the brace. Eq. (1) shows that the force F will be constant if the trajectory of the roller centre verifies that the term A keeps constant. It must be noted that Eq. (1) has been obtained for the upward movement of the rollers, while for the downward displacement the sign preceding μ_r must be changed. This means that, due to friction, the cam can only be designed for an exactly constant force curve in one of the two directions of displacement.

Next, from Eq. (1), the following nonlinear first order differential equation can be derived [24]

$$\frac{\mathrm{d}x}{\mathrm{d}y} = \frac{1-\mu_r f(x)}{\mu_r + f(x)}, \tag{2}$$

where

$$f(x) = \frac{1}{A}(x-x_0) + \frac{x}{l_t}\left(1-\left(\frac{x}{l_t}\right)^2\right)^{-\frac{1}{2}}. \tag{3}$$

To obtain Eq. (2) from Eq. (1), the relations $\tan\beta = \dfrac{\mathrm{d}x}{\mathrm{d}y}$ and $\tan\alpha = \dfrac{x}{l_t}\left(1-\left(\dfrac{x}{l_t}\right)^2\right)^{-\frac{1}{2}}$ have been used. Then, a first order implicit integration formula can be used to solve the differential Eq. (2) [24], resulting in the trajectory of the roller centre.

Finally, the cam profile can be obtained with the CAD software AutoCAD from AUTODESK. First, the points of the roller centre path obtained from the numerical integration are joined by means of a spline. Secondly, the cam curve is obtained using the equidistance tool provided by the software, where the radius of the roller is used for the equidistance.

2.2. Prototype

In order to experimentally validate the design proposed and to analyse its performance, a prototype of the CFM has been elaborated. Fig. 2 shows the CAD model and a picture of the prototype. The cam profile of the mechanism has been designed for a maximum stroke of 250 mm and to achieve a constant force value F of 50 N for a spring stiffness K of 1.38 N/mm. Table 1 summarizes the main characteristics of the CFM. Due to the initial uncertainty of the value of the rolling friction coefficient, the

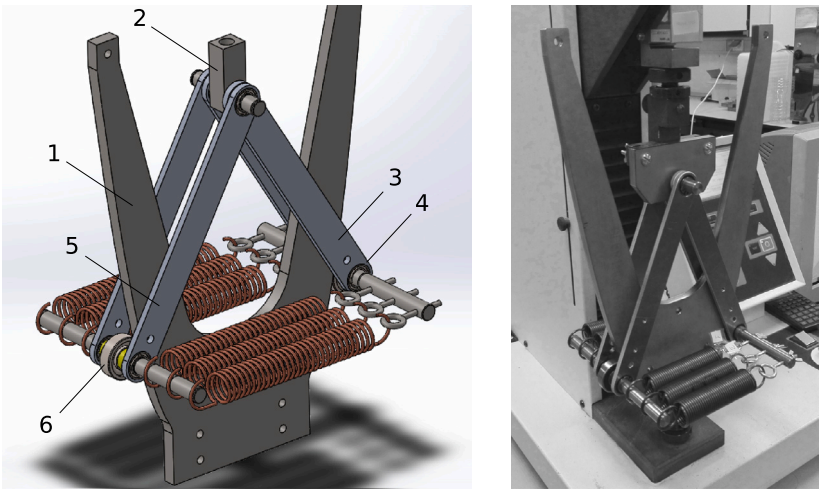

Fig. 2. (a) CAD design of the CFM and (b) an image of the prototype mounted in a H5KS Hounsfield testing machine. Labels in (a): 1 cam, 2 pulling link, 3 and 5 braces (length = 200 mm), 4 and 6 rollers (radius = 16 mm).

Table 1
CFM design parameters.

Constant force, F (see Eq. (1))	$F = 4KA$, with $A = 9.058$
Number of springs in parallel	2/4/6
Possible stiffness, K (N/mm)	1.38/2.76/4.14
Possible force values, F (N)	50/100/150
Stroke (mm)	240
Brace length, l_t (mm)	200
Spring rest length, $2x_o$ (mm)	136
Roller radius, r (mm)	16

cam profile has been derived for $\mu_r = 0$. To achieve a low rolling friction coefficient, the cam is made of stainless steel ASTM A 240 (AISI 304) and two different materials have been tested for the rollers (steel and nylon).

The shaft of the rollers has been prolonged to be able to use up to six springs arranged in parallel. In this way, it is easy to modify the constant force value of the mechanism. According to Eq. (1), the force F is proportional to the spring stiffness. Then, the force value can be changed by adding several springs in parallel or replacing the springs by other with different stiffness constant. In Table 1, three different values of force F are listed (50 N, 100 N, and 150 N), which are achievable by arranging 2, 4, or 6 springs in parallel, with a stiffness of 0.69 N/mm stiffness in each spring. Moreover, others values of force can be obtained using springs with different stiffness. Note that all the springs must have the same rest length, since the distance between the right side and the left side of the cam is conditioned by the spring rest length (defined as $2x_o$ in Fig. 1). To compensate for possible differences in spring length or manufacturing errors, individual spring tensors (M4 × 0.7 mm screws) have been used for each spring to adjust the spring rest length.

2.3. Evaluation of the manufactured cam profile

A precise fabrication of the cam profile is essential to get the constant-force characteristic of the mechanism. The prototype cam has been obtained with a CNC laser cutting machine from the CAD drawing. This manufacturing method has been preferred instead of milling, due to the much lower price of the former. The cam has been obtained from a 10 mm thick steel plate. To evaluate the manufactured cam profile, it has been measured with an optical measuring machine with vision system TESA-VISIO 300 (1 μm resolution) and then compared with the designed profile. Due to the dimensions of the cam and the limited working area of the measuring machine, only the lower half of the cam profile has been measured (first 150 mm of the cam profile). Cam profile measurements were taken at 0.5 mm intervals. The best fit between the set of measured points and the set of model points has been obtained with an iterative closest point (ICP) algorithm, where the registration of the sets of points has been done by iterative reweighted least squares [57]. After the transformation (translation plus rotation) of the measured points sets, a very good fit between both curve points has been obtained, with a root-mean-square error (RMSE) of 0.023 mm and standard deviation (SD) of 0.017 mm. Fig. 3 shows the error in x coordinate between the measured points and the model, for the right and left sides of the cam. Negative values indicate that the measured points of the fabricated cam profile are inside the design profile (lower cam width). These results, which show small manufacturing errors, together with the experimental results described in Section 3, confirm the feasibility of the CNC laser cutting.

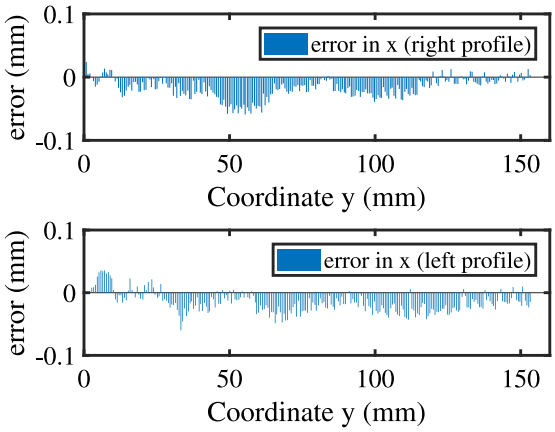

Fig. 3. Error in x coordinate between the measured and the theoretical cam profile.

Table 2
Measured stiffness constant of the springs.

Spring	#1	#2	#3	#4	#5	#6
Stiffness (N/mm)	0.683	0.682	0.681	0.686	0.686	0.679

3. Experimental results

A series of tests have been carried out to analyse the performance of the mechanism. The constant-force mechanism has been tested for three different spring stiffness values and two rollers materials. Previously, some initials tests have been done to obtain the real stiffness constant of the springs and to adjust the spring rest length in the mechanism. All force tests have been done in a H5KS Hounsfield testing machine (see Fig. 2b). This model H5KS includes a 5 kN load cell with a 0.5% load measurement accuracy and 0.001 mm position accuracy. The machine has a maximum stroke of 750 mm and a test speed range from 0.001 mm/min to 1500 mm/min. Tests have been conducted starting with the rollers located at the bottom of the cam and moving upwards. Once the maximum stroke of the mechanism has been reached, with the rollers at the top of the cam, the rollers begin to move downward until they return to the initial position. Most of the tests have been done with a travel speed of 500 mm/min and a sampling rate of 35 Hz.

As described above, the prototype can incorporate up to six springs arranged in parallel (2, 4, or 6 springs are possible). The stiffness of each spring has been obtained through tensile tests. Table 2 lists the stiffness constant values for each spring. The spring rest length will have influence in the force curve of the mechanism, specially in the first section of the cam [24]. For each pair of springs, it has been adjusted the spring rest length from tensile–compression tests results, where the spring rest length can be modified through a screw. Fig. 4 shows the force curves obtained for five different adjustments of the spring rest length of the pair of springs #1 and #2. The step between two consecutive adjustments corresponds to two complete turns of the screw. In Fig. 4, it is represented the upwards and downwards displacements of the mechanism in the same curve, where the resultant hysteresis loop for each test is appreciated. The curve with the best approximation to the constant-force characteristic has been defined as ‘adjust = 0 mm’ in Fig. 4. Variations in the spring rest length result in deviations in the force curve, being more pronounced in the first section of the cam. These results are in accordance with the theoretical results obtained in Ref. [24].

The force value can be modified by adding springs arranged in parallel. Fig. 5 shows the force hysteresis loop measured for 2, 4, and 6 springs. Force curves show some fluctuations due to the errors of the manufactured cam profile and also some noise mainly due to the surface roughness of the cam. In the three force curves, the same fluctuation pattern can be observed. The force curves show larger hysteresis loop for higher spring stiffness, where the area within the hysteresis loop mainly depends on the rolling friction coefficient and the force value. It is interesting to note that the area within the hysteresis loop is not linear with the force (Table 3). For each section of the hysteresis loop (upward and downward displacement), Table 3 summarizes the mean force value, the standard deviation and the maximum and minimum values. Additionally, it is included the theoretical value of the forces, calculated from Eq. (1) with the measured spring stiffness constant and for null friction coefficient. These force values have been represented with dashed lines in Fig. 5.

All force curves obtained in the different tests showed high repeatability. As example, Fig. 6 shows five repetitions of the force test for four springs in parallel.

The tests described so far have been done with rollers of steel. With the aim of studying the effect of other materials in the rolling friction, rollers of nylon have been tested. The curves for the three force levels obtained for steel rollers have been compared with the curves obtained for nylon rollers, showing small differences between the curves. As expected, since the rolling friction for nylon material is slightly higher, the hysteresis loop is somewhat larger when nylon rollers are used. This difference is more easily

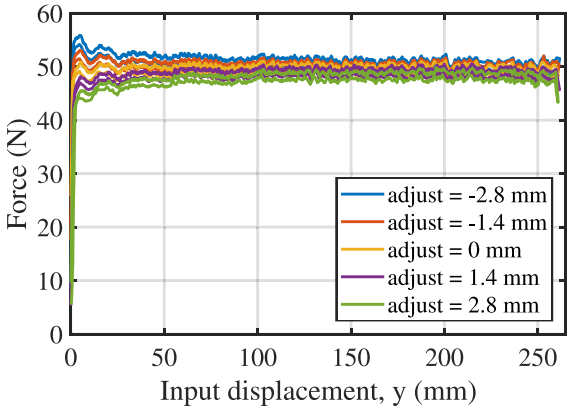

Fig. 4. Force curves for variations in the spring rest length.

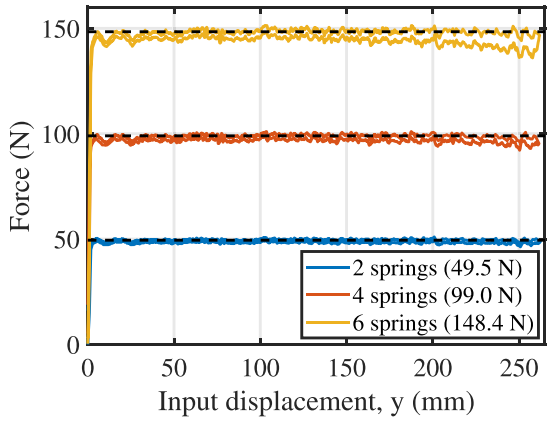

Fig. 5. Force curves for 2, 4, and 6 springs in parallel.

Table 3
Parameters of the force curves in Fig. 5.

Springs arranged in parallel	2 (#1 and #2)	4 (#1 to #4)	6 (#1 to #6)
Spring equivalent stiffness (N/mm)	1.365	2.732	4.097
Theoretical force (N)	49.46	98.99	148.4
Displacement	up/down	up/down	up/down
Mean force (N)	49.67/48.27	98.94/96.62	148.27/144.17
Standard deviation (N)	0.427/0.425	0.949/1.02	1.38/2.12
Max. force (N)	51.00/49.33	101.0/99.00	151.33/148.00
Min. force (N)	48.00/46.33	95.33/92.17	143.17/136.00
Hysteresis loop area (N m)	0.406	0.555	1.069

observed in the curves of higher value of force. Fig. 7 shows the curve force for the two type of rollers and for 6 springs, with hysteresis loop areas of 1.069 Nm and 1.220 Nm for steel and nylon rollers, respectively.

Test displacement speed may influence the force curve results. Previous results were conducted at 500 mm/min. Next, Fig. 8 shows the force curves for five different velocities, from 100 mm/min to 1500 mm/min (maximum allowed by the testing machine). Since the displacement velocity is low in all tests, no appreciable influence of inertia forces is expected. All curves show the same main fluctuation due to the small deviation in the manufacturing process, but the noise due to surface roughness increases with decreasing speed. As representative values, the standard deviations for the upward displacement section of the curves are 0.693 N, 0.551 N, 0.427 N, 0.359 N and 0.318 N for the velocities between 100 mm/min and 1500 mm/min shown in Fig. 8.

Finally, this section presents a comparison between experimental results and simulations using the measured cam profile described in Section 2.3. The simulations were performed with SOLIDWORKS motion commercial software, which uses the ADAMS/Solver simulation engine to solve the equations of motion and calculate the forces on each component of the assembly. The real model has been simplified for simulations. Braces, springs and shafts have been included as virtual links without mass. In addition, no mass has been considered for the rollers. Therefore, no inertial effects are considered, which have no significant

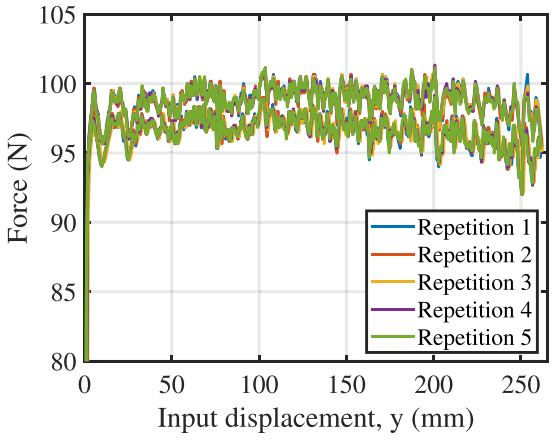

Fig. 6. Force curves for five repetitions of the force test (4 springs).

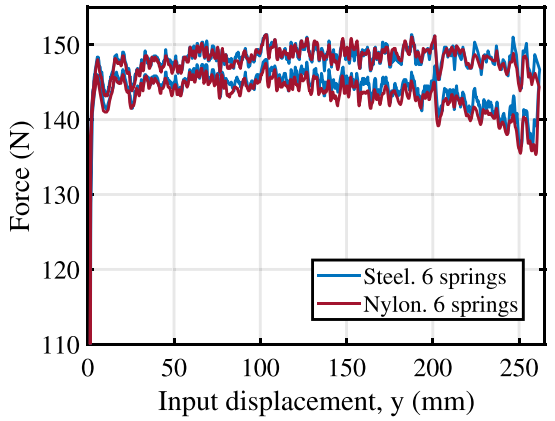

Fig. 7. Force curves for steel rollers and for nylon rollers (6 springs).

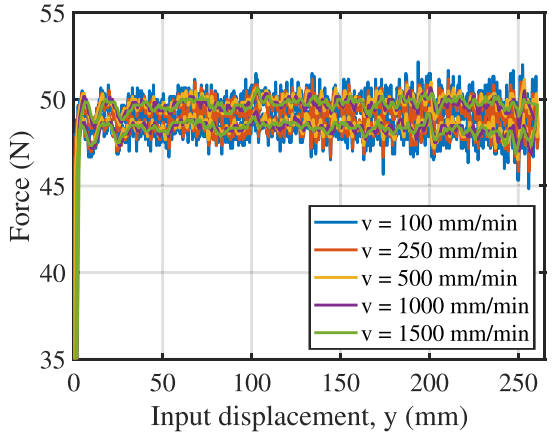

Fig. 8. Force curves for different displacement velocities (2 springs).

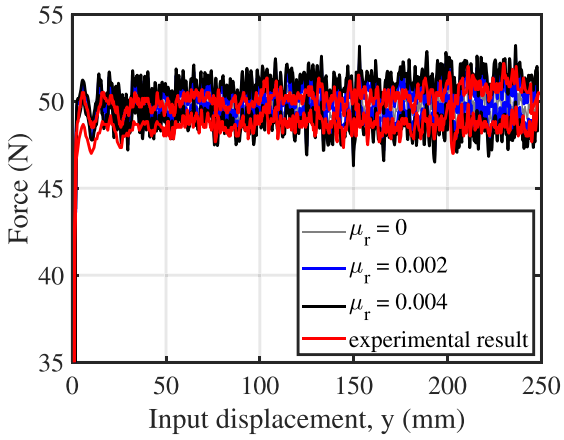

(a)

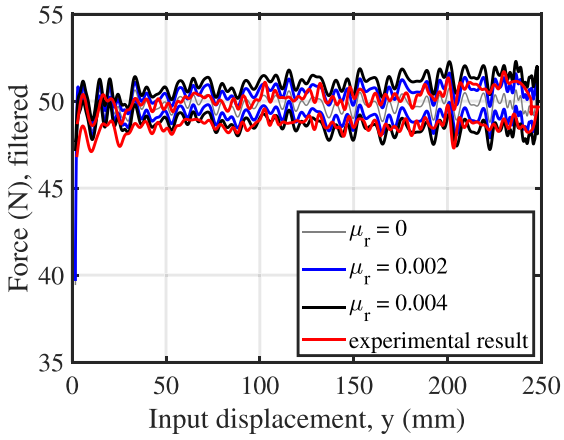

(b)

Fig. 9. Force curves from experimental result and from simulations with the measured cam profile and different values of the rolling friction coefficient. (a) raw data and (b) filtered curves.

influence due to the low accelerations. As in the tests, the simulations were performed with a low displacement velocity of 500 mm/min. Lastly, the contacts between the rollers and the measured cam profile have been imposed as non-penetrating and with allowable separation, and the rolling friction coefficient μ_r has been included.

Fig. 9(a) shows the measured force as well as the simulated results for rolling friction coefficient values of $\mu_r = 0.002$ and $\mu_r = 0.004$, and for no friction. For an easier comparison of the results, the data reported in Fig. 9(a) have been back and forth filtered with a sixth order Butterworth filter with cut-off frequency of 2 Hz, leading to the smoother curves drawn in Fig. 9 (b). From the similarity in the fluctuations shown in the experimentally measured and simulated curves, it is confirmed that the force fluctuations are due to manufacturing errors. The error induced by the machining process defined as the difference between the force measured in the test conducted on the manufactured mechanism and the force obtained by simulation using the profile sent to the manufacturer is studied later on in Section 4, where a dedicated multibody model of the CFM mechanism is developed. Besides the similarity of the curves, a drop in the experimental curve with respect to the simulated curves can be appreciated in the initial section of the displacement. This may be indicative that the spring rest length introduced in the simulation (the theoretical one) does not fit the real one (see Fig. 4). In Fig. 10, the simulation has been repeated for $\mu_r = 0.002$, but a spring rest length of 136.5 mm (0.5 mm longer than the theoretical) has been used instead. In this way, the simulated curves of Fig. 10 follow a more similar pattern in the initial section.

In addition, the results of the simulations allow obtaining an indicative value of the rolling friction coefficient. In Fig. 9(a), the areas of the hysteresis loops in the section between 40 mm and 210 mm of the input displacement result in 0.233 Nm and 0.410 Nm for $\mu_r = 0.002$ and $\mu_r = 0.004$, respectively, and 0.259 Nm for the experimental measurement. In Fig. 10(a), for $\mu_r = 0.002$, the area is 0.232 Nm (almost the same as for Fig. 9(a)). These values indicate that, for this case, the real rolling friction coefficient will be slightly higher than 0.002. Once the value of the rolling friction coefficient has been identified, the cam profile could be designed

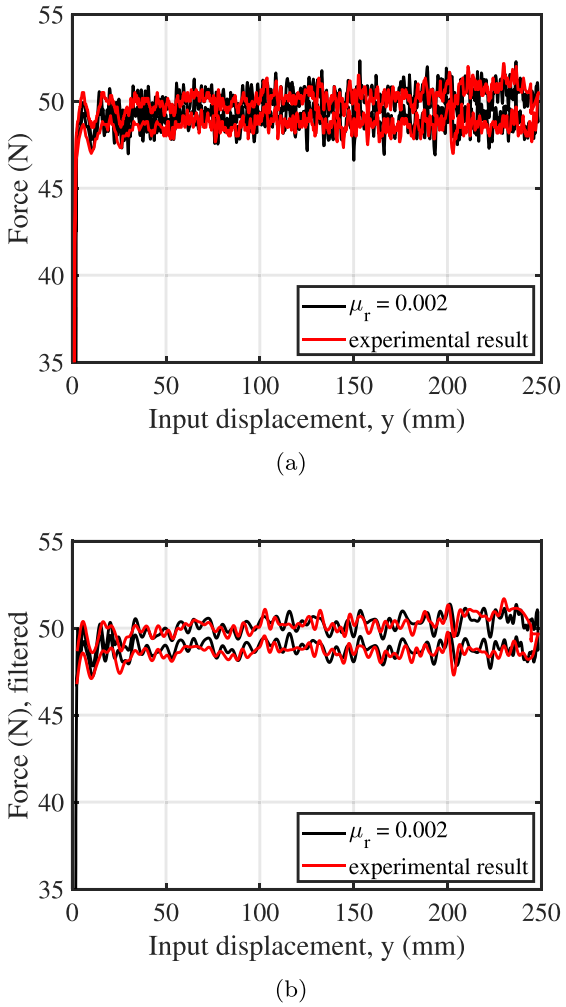

Fig. 10. Force curves from experimental result and from simulation with the measured cam profile, a spring rest length of 136.5 mm and a rolling friction coefficient of 0.002. (a) raw data and (b) filtered curves.

by including that value in Eq. (1). This allows maintaining a more accurate constant force curve in one of the directions of the displacement.

4. Multibody model of the CFM mechanism

The objective of this section is to develop a multibody model of the CFM that reproduces the experimental results presented before. Once the model is validated by comparison with the experimental results, it will be used to investigate the influence of inertial effects and manufacturing tolerances on the CFM performance.

In order to be able to study a wide range of manufacturing errors, the mathematical model of the CFM does not make use of symmetry. Instead, the two cam profiles of the CMF are modelled separately. The model comprises a total of five moving bodies which are described as follows (see Fig. 11). Body 2 is a slider that translates vertically when pulled up by the user. It is the input body of the mechanism. Both bodies 3 and 5 are connecting rods articulated to the slider and the two rollers, bodies 4 and 6, which are assumed to roll without slipping over the left and right cam surfaces. The assumption of no slipping is reasonable as long as the rollers have low inertia torques and low friction torques. They just follow the cam profile as the slider is pulled upwards.

Since the cam profile has a curved shape, the contact between the roller and the cam is implemented by using two non-generalized coordinates to locate the contact point of each roller. The vector of coordinates is as follows:

$$\boldsymbol{x} = \begin{pmatrix} s_2 & \theta_3 & \theta_4 & \xi_4 & y_4 & \theta_5 & \theta_6 & \xi_6 & y_6 \end{pmatrix}^{\mathrm{T}}, \tag{4}$$

where ξ_4 and y_4 are the non-generalized coordinates used to define the contact of roller 4 and the right cam profile, and ξ_6 and y_6 are the non-generalized coordinates used to define the contact of roller 6 and the left cam profile. This set of coordinates is

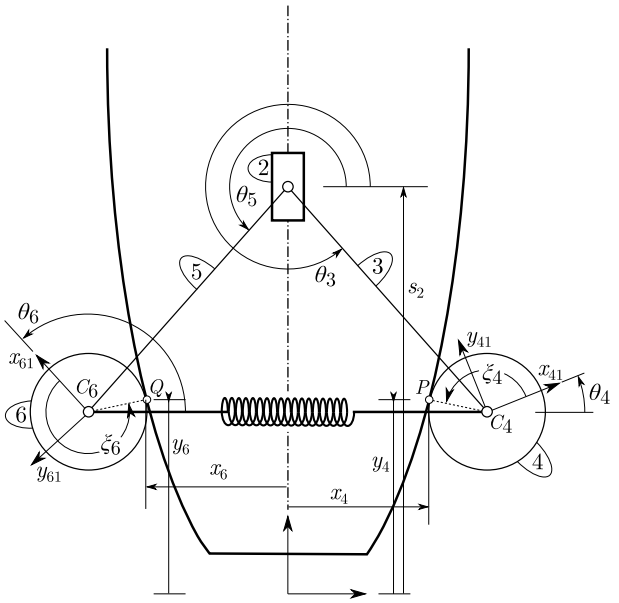

Fig. 11. Sketch of the mathematical model of the constant force mechanism.

constrained by eight constraints (six holonomic plus two velocity constraints). The holonomic constraints are as follows:

$$\boldsymbol{c}_h(\boldsymbol{x}) = \begin{pmatrix} \boldsymbol{r_2} + \boldsymbol{r_3} + \boldsymbol{C_4P} - \boldsymbol{r_1^P} \\ \boldsymbol{t_1^P} \cdot \boldsymbol{C_4P} \\ \boldsymbol{r_2} + \boldsymbol{r_5} + \boldsymbol{C_6Q} - \boldsymbol{r_1^Q} \\ \boldsymbol{t_1^Q} \cdot \boldsymbol{C_6Q} \end{pmatrix} = \boldsymbol{0}_{6\times 1}, \tag{5}$$

with

$$\boldsymbol{r_1^P} = \begin{pmatrix} x_4(y_4) & y_4 & 0 \end{pmatrix}^{\mathrm{T}}, \tag{6}$$

$$\boldsymbol{r_2} = \begin{pmatrix} 0 & s_2 & 0 \end{pmatrix}^{\mathrm{T}}, \tag{7}$$

$$\boldsymbol{r_3} = \begin{pmatrix} L_3\cos\theta_3 & L_3\sin\theta_3 & 0 \end{pmatrix}^{\mathrm{T}}, \tag{8}$$

$$\boldsymbol{C_4P} = \begin{pmatrix} R_4\cos\left(\theta_4+\xi_4\right) & R_4\sin\left(\theta_4+\xi_4\right) & 0 \end{pmatrix}^{\mathrm{T}}, \tag{9}$$

$$\boldsymbol{r_1^Q} = \begin{pmatrix} x_6(y_6) & y_6 & 0 \end{pmatrix}^{\mathrm{T}}, \tag{10}$$

$$\boldsymbol{r_5} = \begin{pmatrix} L_5\cos\theta_5 & L_5\sin\theta_5 & 0 \end{pmatrix}^{\mathrm{T}}, \tag{11}$$

$$\boldsymbol{C_6Q} = \begin{pmatrix} R_6\cos\left(\theta_6+\xi_6\right) & R_6\sin\left(\theta_6+\xi_6\right) & 0 \end{pmatrix}^{\mathrm{T}}, \tag{12}$$

where L_3 and L_5 are the lengths of the bodies 3 and 5, respectively, and R_4 and R_6 are the radii of the rollers 4 and 6. Moreover, $\boldsymbol{t_1^P}$ and $\boldsymbol{t_1^Q}$ are two vectors tangent to the right and left cam profiles at contact points P and Q, respectively. Note that $x_4(y_4)$ and $x_6(y_6)$ are expressed explicitly as functions of y_4 and y_6, respectively. Vectors $\boldsymbol{t_1^P}$ and $\boldsymbol{t_1^Q}$ are calculated from the known functions of the cam profiles, $x_4 = x_4(y_4)$ and $x_6 = x_6(y_6)$, as follows:

$$\boldsymbol{t_1^P} = \frac{\mathrm{d}\boldsymbol{r_1^P}}{\mathrm{d}y_4} = \begin{pmatrix} \dfrac{\mathrm{d}x_4\left(y_4\right)}{\mathrm{d}y_4} & 1 & 0 \end{pmatrix}^{T}, \tag{13}$$

$$\boldsymbol{t_1^Q} = \frac{\mathrm{d}\boldsymbol{r_1^Q}}{\mathrm{d}y_6} = \begin{pmatrix} \dfrac{\mathrm{d}x_6\left(y_6\right)}{\mathrm{d}y_6} & 1 & 0 \end{pmatrix}^{T}. \tag{14}$$

In addition, two velocity constraints expressing the rolling without slipping contacts are added as follows

$$\boldsymbol{c}_{nh}(\boldsymbol{x}, \dot{\boldsymbol{x}}) = \begin{pmatrix} \boldsymbol{t_1^P} \cdot \left(\dot{\boldsymbol{r}}_4^{C4} + \boldsymbol{\omega_4} \times \boldsymbol{C_4P}\right) \\ \boldsymbol{t_1^Q} \cdot \left(\dot{\boldsymbol{r}}_6^{C6} + \boldsymbol{\omega_6} \times \boldsymbol{C_6Q}\right) \end{pmatrix} = \boldsymbol{0}_{2\times 1}, \tag{15}$$

where $\dot{\boldsymbol{r}}_4^{C4}$ and $\dot{\boldsymbol{r}}_6^{C6}$ are the absolute velocities of the rollers' centres. Note that the previous equations are linear in the velocities and they can be expressed as $\boldsymbol{c}_{nh}(\boldsymbol{x}, \dot{\boldsymbol{x}}) = \boldsymbol{B}(\boldsymbol{x})\,\dot{\boldsymbol{x}}$, being $\boldsymbol{B}(\boldsymbol{x})$ a coordinate dependent 2×9 matrix.

In order to perform the simulations, the motion of the slider, Body 2, is prescribed through the introduction of the following rheonomic constraint:

$$c_{rh}(\boldsymbol{x}, t) = s_2 - f(t), \tag{16}$$

being $f(t)$ defined by the following cycloidal displacement profile:

$$f(t) = s_2^0 + A\left(\frac{t}{T} - \frac{1}{2\pi}\sin\left(\frac{2\pi t}{T}\right)\right), \tag{17}$$

where s_2^0 is the vertical initial position of the slider, the parameter T is used to control the speed of the exercise and A is the vertical stroke of the slider. The cycloidal profile has been selected in order to start and end the elevation of the slider at zero velocity and zero acceleration. Observe that by adding the last rheonomic constraint, the kinematics and the dynamics of the mechanism can be solved as follows:

1. Find an admissible initial position coordinate vector, $\boldsymbol{x_0}$, by solving the six holonomic constraints as follows:

$$\boldsymbol{c}_h\left(\boldsymbol{x_0}\right) = \boldsymbol{0}_{6\times 1} \quad \text{for} \quad \begin{matrix} s_2(0) = s_2^0 \\ \xi_4(0) = \pi \\ \xi_6(0) = 0 \end{matrix} \tag{18}$$

   where three out of nine coordinates can be prescribed.
2. Numerically integrate the following system of first order differential equations:

$$\dot{\boldsymbol{c}}_h(\boldsymbol{x}) + \beta \boldsymbol{c}_h(\boldsymbol{x}) = \boldsymbol{0}_{6\times 1}, \tag{19}$$

$$\boldsymbol{B}(\boldsymbol{x})\,\dot{\boldsymbol{x}} = \boldsymbol{0}_{2\times 1}, \tag{20}$$

$$\dot{c}_{rh}(\boldsymbol{x}, t) + \beta c_{rh}(\boldsymbol{x}, t) = 0_{1\times 1}, \tag{21}$$

$$\boldsymbol{x}(0) = \boldsymbol{x_0}, \tag{22}$$

   where β is a positive parameter introduced to stabilize the holonomic and the rheonomic constraints during numerical integration according to Baumgarte's method [58]. Note that, in order to find a first order differential system, both the holonomic and the rheonomic constraints have been differentiated with respect to time. Therefore, if no means were taken to prevent the numerical drift due to the integration, the results could be completely useless. Introducing the holonomic constraints as in Eq. (19) and the rheonomic constraint as in Eq. (21), one may use a conventional numerical integrator avoiding constraint violations. As a result of this step, one finds the trajectories and velocities from initial time to time T.
3. Differentiate the holonomic and rhenomic constraints twice with respect to time and the velocity constraints once with respect to time to find a system of 9 equations in which the acceleration vector, $\ddot{\boldsymbol{x}}$, is the unknown as follows:

$$\frac{\partial \boldsymbol{c}_h(\boldsymbol{x})}{\partial \boldsymbol{x}}\ddot{\boldsymbol{x}} + \frac{\partial}{\partial \boldsymbol{x}}\left(\frac{\partial \boldsymbol{c}_h(\boldsymbol{x})}{\partial \boldsymbol{x}}\dot{\boldsymbol{x}}\right)\dot{\boldsymbol{x}} = \boldsymbol{0}_{6\times 1}, \tag{23}$$

$$\boldsymbol{B}(\boldsymbol{x})\,\ddot{\boldsymbol{x}} + \frac{\partial}{\partial \boldsymbol{x}}\left(\boldsymbol{B}(\boldsymbol{x})\,\dot{\boldsymbol{x}}\right)\dot{\boldsymbol{x}} = \boldsymbol{0}_{2\times 1}, \tag{24}$$

$$\frac{\partial \boldsymbol{c}_{rh}(\boldsymbol{x}, t)}{\partial \boldsymbol{x}}\ddot{\boldsymbol{x}} + \frac{\partial}{\partial \boldsymbol{x}}\left(\frac{\partial \boldsymbol{c}_{rh}(\boldsymbol{x}, t)}{\partial \boldsymbol{x}}\dot{\boldsymbol{x}}\right)\dot{\boldsymbol{x}} + 2\frac{\partial^2 \boldsymbol{c}_{rh}(\boldsymbol{x}, t)}{\partial \boldsymbol{x}\partial t}\dot{\boldsymbol{x}} + \frac{\partial^2 \boldsymbol{c}_{rh}(\boldsymbol{x}, t)}{\partial t^2} = \boldsymbol{0}_{1\times 1}, \tag{25}$$

4. Knowing the positions, velocities and accelerations of the mechanism, use the equations of motion to find a set of 9 Lagrange multipliers as follows:

$$\boldsymbol{m}(\boldsymbol{x})\,\ddot{\boldsymbol{x}} + \boldsymbol{D}^T(\boldsymbol{x}, t)\,\lambda = \boldsymbol{q}(\boldsymbol{x}, \dot{\boldsymbol{x}}) \tag{26}$$

   where $\boldsymbol{m}(\boldsymbol{x})$ is the 9×9 system mass matrix, $\boldsymbol{q}(\boldsymbol{x}, \dot{\boldsymbol{x}})$ is the 9×1 generalized applied force vector, which includes gravity forces, λ is the 9×1 Lagrange multipliers vector and $\boldsymbol{D}(\boldsymbol{x}, t)$ is the 9×9 constraints' Jacobian, which is built as follows:

$$\boldsymbol{D}(\boldsymbol{x}, t) = \begin{pmatrix} \dfrac{\partial \boldsymbol{c}_h(\boldsymbol{x})}{\partial \boldsymbol{x}} \\ \boldsymbol{B}(\boldsymbol{x}) \\ \dfrac{\partial \boldsymbol{c}_{rh}(\boldsymbol{x}, t)}{\partial \boldsymbol{x}} \end{pmatrix}. \tag{27}$$

   Since the mechanism is kinematically driven, the Jacobian of the constraints is a full rank square matrix and the Lagrange multipliers are evaluated by inverse dynamics analysis at any time t as follows:

$$\lambda = \left(\boldsymbol{D}^T(\boldsymbol{x}, t)\right)^{-1}\left(\boldsymbol{q}(\boldsymbol{x}, \dot{\boldsymbol{x}}) - \boldsymbol{m}(\boldsymbol{x})\,\ddot{\boldsymbol{x}}\right). \tag{28}$$

   Finally, the external force required to move the slider, Body 2, according to Eq. (16) is found from the value of the ninth Lagrange multiplier with opposite sign.

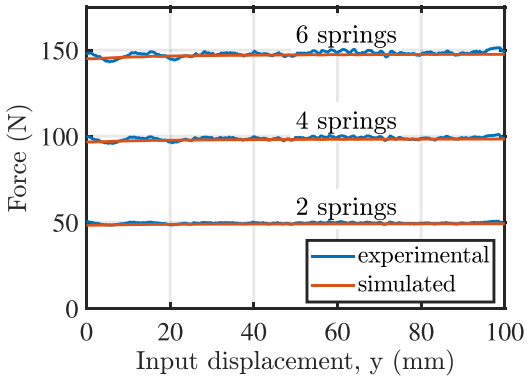

Fig. 12. Comparison of the simulated and experimental results.

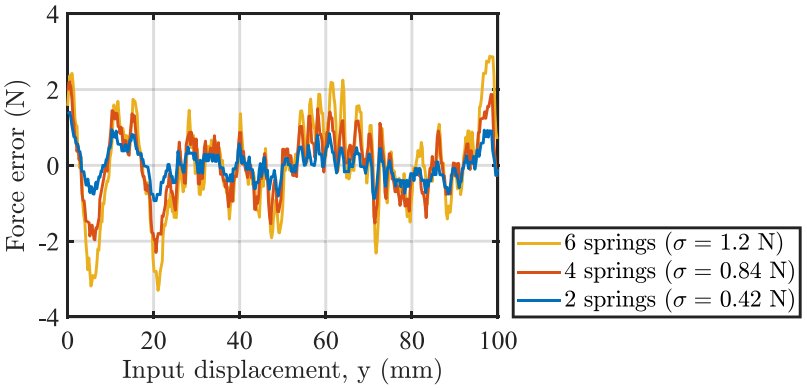

Fig. 13. Analysis of the error in the input force due to the manufacturing process.

Following the previous procedure, the performance of the CFM mechanism, whose design parameters were summarized in Table 1, has been simulated. The measured masses and moments of inertia of the different bodies are: $m_2 = 0.068$ kg, $m_3 = m_5 = 0.077$ kg, $m_4 = m_6 = 0.38$ kg, $I_{G3} = I_{G5} = 2.57 \cdot 10^{-4}$ kg m^2 and $I_{G4} = I_{G6} = 4.61 \cdot 10^{-6}$ kg m^2. In the simulation, the designed cam profile was utilized, which is obviously absent of manufacturing errors. Since the designed profile is obtained by following the numerical procedure described in Section 2.1, the derivatives of the cam profile need to be evaluated numerically, too. To that end, a second order finite difference formula has been used. The obtained derivatives have been low pass filtered to avoid oscillations due to numerical differentiation. The simulation has been conducted starting with a value of s_2^0 of 206.5 mm for a stroke of 100 mm. Eqs. (19)–(21) have been integrated using a conventional fourth order Runge–Kutta method.

The results of the simulations are compared with the experimental ones in Fig. 12. It can be observed that the numerical multibody model captures quite well the behaviour of the CFM mechanism for the three settings selected. The comparison shows a very good agreement in a large part of the simulated stroke. However, there are appreciable differences at the beginning of the stroke that are attributed to manufacturing errors. Such differences are studied and quantified next.

In order to assess the error induced in the input force by the machining process, the difference between the experimental input force and the simulated input force has been analysed and plot in Fig. 13. Note that the simulation is based on the designed cam profile, which was sent to the manufacturer. Therefore, such error force is attributed to deviations of the real cam profile from the designed one due to manufacturing. As shown in Fig. 13, the error increases with the stiffness of the springs set. The standard deviation of the error along the simulated stroke for each set of springs is included in the figure legend. In all cases the standard deviation is approximately 0.8% of the target load.

5. Sensitivity analysis

Once the multibody model has shown a good fit with the experimental results, it is used in this section to study the influence of some decisive design parameters of the CFM, as well as some possible manufacturing or assembly errors, following the previously described solution procedure. The first analysis carried out is aimed at studying the influence of the inertial forces on the force required for the slider to follow the cycloidal profile of Eq. (17), with $A = 100$ mm, starting at $s_2^0 = 220$ mm. The total time taken to elevate the slider, T, is varied from 0.125 s to 1 s, thus generating different acceleration peaks. The results are shown in Fig. 14, where it can be seen that the inertial effects become significant for small enough values of T. The results show that for the set of

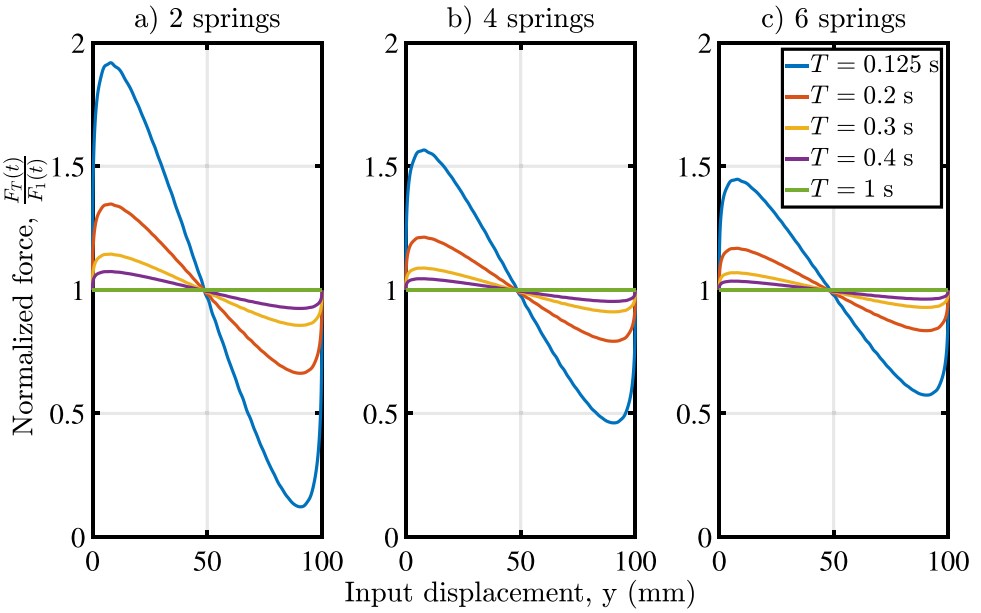

Fig. 14. Analysis of the inertial effect on the CFM response. The normalized force, $F_T(t)/F_1(t)$, is calculated by dividing the input force for an execution time T, $F_T(t)$, by the input force for an execution time of 1 s, $F_1(t)$, for which the inertial effect are negligible.

parameters studied, a reduction of the execution time, T, leads to significant variations of the input force required to perform the stroke following the cycloidal profile. Thus, reducing T from 1 s to 0.125 s results in peaks of the input force of 91.8%, 56.6% and 44.7% for the 2 springs, 4 springs and 6 springs sets, respectively. Remarkably, the influence of the inertial effects becomes less important as the design input force increases. As a mean of comparison, it may be considered that lifting an equivalent death weight following the same cycloidal profile results in peaks that are $\max[\ddot{s}_2(t)]/g$ times larger than the moved weight. This means an increase of 310% for $T = 0.125$ s. Therefore, while the CFM is sensitive to the inertial forces, it shows a more stable input force when compared to a pure weight lifting.

Using the cycloidal lifting profile, an execution time of 0.125 s during a stroke of 0.1 m results in a mean velocity of 0.8 m/s and a maximum velocity of 1.6 m/s, which are values close to those of a typical 60% of 1 RPM execution of bench press exercise according to the literature [59,60].

The CFM is designed for the slider to move along the symmetry axis of the cam. Nevertheless, deviations may occur during the mechanism actuation, as could occur in the case of cable actuation in bodybuilding machines. Therefore, it is interesting to study the influence of a deviation of the slider trajectory from its designed one. The calibrated CFM model has been used to simulate the values of the input force required to move the slider along a cycloidal profile with $A = 100$ mm, $s_2^0 = 212$ mm and $T = 10$ s for different values of the angle of deviation of the slider trajectory. To that end, the cam profiles have been rotated an angle α around the coordinate point (0,0). The results are shown in Fig. 15 for α values from 0° to 5°. Notice that the results are equal no matter the angle α is rotated clockwise or counter clockwise. It can be seen that the load increases significantly during a 100 mm stroke. This allows identifying the importance of caring about the inclination of the input force. The results show that the input load may increase as much as a 20% of the design input force for a deviation of 5°.

Finally, a possible manufacturing error is investigated. In this case, it will be assumed that the profile has been cut so that the cam profiles are rotated symmetrically an angle α around the coordinate point (0,0). This results in the horizontal width of the cam varying linearly from bottom to top with respect to the design profile. The calibrated CFM model has been used to simulate the values of the input force required to move the slider along a cycloidal profile with $A = 100$ mm, $s_2^0 = 220$ mm and $T = 10$ s for different values of the angle α. The results are shown in Fig. 16 for α values from −0.4° to 0.4°. It can be observed that the load varies during a 100 mm stroke. The results show that the input load may increase about an 8% of the design input force for a manufacturing error of 0.4°. According to this simulation, performing a high quality cut of the cam becomes highly important.

6. Summary and conclusions

The design of the constant-force mechanism manufactured has demonstrated good performance with respect to the primary feature of constant force. The design of the mechanism, based on springs and cams, allows achieving large strokes and a changeable force level. The main factors that affect the ideal constant force curve are the friction between the rolling elements and the manufacturing process. Frictional forces inevitably lead to hysteresis loops. In spite of this hysteresis, by identifying the value of the rolling friction coefficient, the cam profile could be designed for a more precise constant force in one of the displacement directions.

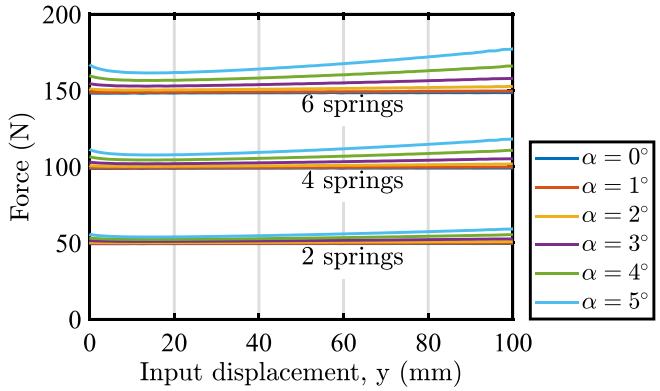

Fig. 15. Analysis of the influence of the slider misalignment on the CFM response.

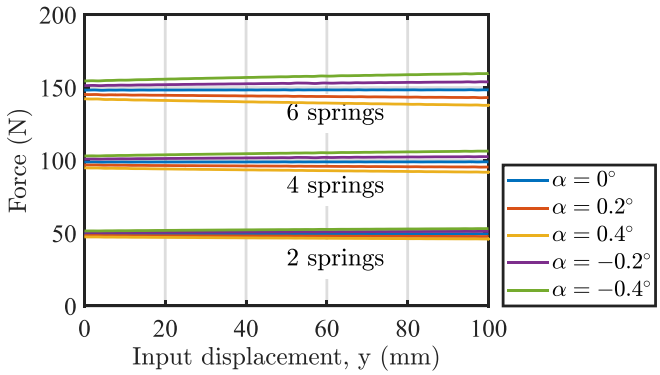

Fig. 16. Analysis of an angular manufacturing defect on the CFM response.

Surface irregularities in the cam surface due to the laser cutting manufacturing process cause noise in the force curve. However, if required, these irregularities could be avoided with more precise manufacturing by CNC milling. Some fluctuations in the force curve, that are present in the experimental results but are absent in the multibody simulation following the design cam profile, could be identified to being caused by an imprecise manufacture of the cam profile.

An ad-hoc multibody model of the CFM has been developed and validated against the experimental results presented in this paper. Thus, by using the multibody model of the CFM, relevant conclusions could be drawn on the influence of the inertial effects, a typical execution error and a possible manufacturing error. In this way, it could be concluded that, by reducing the execution time, T, significant variations of the input force required to perform the stroke following the cycloidal profile may arise. Nevertheless, the analysed CFM shows a much less sensitive behaviour than the pure weight lifting. Therefore, it is an excellent candidate to design training or rehabilitating exercise machines where the resistant force should be as constant as possible.

The simulations also revealed a significant influence of possible manufacturing errors as a linear deviation of the cam profiles. Therefore, controlling the quality of the cam profile becomes highly important. In addition, the simulation showed that significant variations of the input force may arise as a consequence of a deviation in the slider trajectory. Therefore, the importance of caring about the inclination of the input force during the mechanism stroke is clearly identified.

Finally, the multibody model will be useful in the design of future CFMs. Thus, the design and fabrication of a full-scale CFM to be incorporated into a body-building machine is planned for the future.

Declaration of competing interest

The authors declare that they have no known competing financial interests or personal relationships that could have appeared to influence the work reported in this paper.

Acknowledgements

This work has been partially funded by the "Programa Operativo FEDER, Spain 2014–2020" and the Andalusian "Consejería de Transformación Económica, Industria, Conocimiento y Universidades, Spain" under the project UAL2020-CTS-A2100, and supported by Grant FPU18/05598 of the Spanish Ministry of Science, Innovation and Universities.

References

[1] P. Wang, Q. Xu, Design and modeling of constant-force mechanisms: A survey, Mech. Mach. Theory 119 (2018) 1–21, http://dx.doi.org/10.1016/j.mechmachtheory.2017.08.017.
[2] L. Howell, Compliant Mechanisms, John Wiley Sons, New York, 2001.
[3] J. Gallego, J. Herder, Classification for literature on compliant mechanisms: A design methodology based approach, in: Proceedings of the ASME International Design Engineering Technical Conferences and Computers and Information in Engineering Conference 2009, DETC2009, Vol. 7 PART A, 2010, pp. 289–297.
[4] Y. Tian, C. Zhou, F. Wang, K. Lu, D. Zhang, A novel compliant mechanism based system to calibrate spring constant of AFM cantilevers, Sensors Actuators A 309 (2020) 112027.
[5] K. Tolman, E. Merriam, L. Howell, Compliant constant-force linear-motion mechanism, Mech. Mach. Theory 106 (2016) 68–79.
[6] J. Meaders, C. Mattson, Optimization of near-constant force springs subject to mating uncertainty, Struct. Multidiscip. Optim. 41 (1) (2010) 1–15.
[7] H. Prakashah, H. Zhou, Synthesis of constant torque compliant mechanisms, J. Mech. Robot. 8 (6) (2016).
[8] C.-H. Liu, F.-M. Chung, Y.-P. Ho, Topology optimization for design of a 3D-printed constant-force compliant finger, IEEE/ASME Trans. Mechatronics (2021).
[9] B. Ding, X. Li, Y. Li, FEA-based optimization and experimental verification of a typical flexure-based constant force module, Sensors Actuators A 332 (2021) 113083.
[10] A. Lamers, J. Gallego Sánchez, J. Herder, Design of a statically balanced fully compliant grasper, Mech. Mach. Theory 92 (2015) 230–239.
[11] C. Boyle, L. Howell, S. Magleby, M. Evans, Dynamic modeling of compliant constant-force compression mechanisms, Mech. Mach. Theory 38 (12) (2003) 1469–1487.
[12] P. Bilancia, G. Berselli, Design and testing of a monolithic compliant constant force mechanism, Smart Mater. Struct. 29 (4) (2020) 044001.
[13] Y. Tian, C. Zhou, F. Wang, K. Lu, Y. Yuan, M. Yang, D. Zhang, Design of a flexure-based mechanism possessing low stiffness and constant force, Rev. Sci. Instrum. 90 (10) (2019) 105005.
[14] Y. Liu, D.-P. Yu, J. Yao, Design of an adjustable cam based constant force mechanism, Mech. Mach. Theory 103 (2016) 85–97.
[15] M. Li, W. Cheng, Design and experimental validation of a large-displacement constant-force mechanism, J. Mech. Robot. 10 (5) (2018) 051007.
[16] I. Gandhi, H. Zhou, Synthesizing constant torque compliant mechanisms using precompressed beams, J. Mech. Des. 141 (1) (2019) 014501.
[17] H.-T. Pham, D.-A. Wang, A constant-force bistable mechanism for force regulation and overload protection, Mech. Mach. Theory 46 (7) (2011) 899–909.
[18] P. Wang, Q. Xu, Design of a flexure-based constant-force XY precision positioning stage, Mech. Mach. Theory 108 (2017) 1–13.
[19] T. Ye, J. Ling, X. Kang, Z. Feng, X. Xiao, A novel two-stage constant force compliant microgripper, J. Mech. Des. 143 (5) (2021) 053302.
[20] Y.-L. Kuo, C.-C. Lan, A two-dimensional adjustable constant-force mechanism, J. Mech. Des. 142 (6) (2020).
[21] Y. Liu, Y. Zhang, Q. Xu, Design and control of a novel compliant constant-force gripper based on buckled fixed-guided beams, IEEE/ASME Trans. Mechatronics 22 (1) (2017) 476–486.
[22] X. Liu, X. Huang, H. Hua, On the characteristics of a quasi-zero stiffness isolator using Euler buckled beam as negative stiffness corrector, J. Sound Vib. 332 (14) (2013) 3359–3376.
[23] F. Ma, G. Chen, H. Wang, Large-stroke constant-force mechanisms utilizing second buckling mode of flexible beams: Evaluation metrics and design approach, J. Mech. Des. 142 (10) (2020) 103303.
[24] J. López-Martínez, D. García-Vallejo, F. Arrabal-Campos, J. García-Manrique, Design of three new cam-based constant-force mechanisms, Trans. ASME, J. Mech. Des. 140 (8) (2018) http://dx.doi.org/10.1115/1.4040174.
[25] M. Li, W. Cheng, R. Xie, Design and experimental validation of a cam-based constant-force compression mechanism with friction considered, Proc. Inst. Mech. Eng. C 233 (11) (2019) 3873–3887.
[26] R. Nathan, A constant force generation mechanism, Trans. ASME, J. Mech. Des. 107 (4) (1985) 508–512, http://dx.doi.org/10.1115/1.3260755.
[27] Z.-W. Yang, C.-C. Lan, An adjustable gravity-balancing mechanism using planar extension and compression springs, Mech. Mach. Theory 92 (2015) 314–329.
[28] G. Endo, H. Yamada, A. Yajima, M. Ogata, S. Hirose, A passive weight compensation mechanism with a non-circular pulley and a spring, in: Proceedings - IEEE International Conference on Robotics and Automation, 2010, pp. 3843–3848.
[29] M. French, M. Widden, The spring-and-lever balancing mechanism, George Carwardine and the Anglepoise lamp, Proc. Inst. Mech. Eng. C 214 (3) (2000) 501–508.
[30] E. Starostin, Calculating a cam profile for a constant-force mechanism, Sov. Mach. Sci. (4) (1987) 69–76.
[31] E. Duval, Dual pulley constant force mechanism, 2010, US Patent 7,677,540.
[32] G. Keung, C. Chen, Novel design of an adjustable constant force mechanism based on cam and spring, in: IFToMM World Congress on Mechanism and Machine Science, Springer, 2019, pp. 1481–1490.
[33] Q. Xie, S. Liu, H. Jiang, Design of a passive constant-force mechanism based on a five-bar mechanism, Mech. Mach. Theory 143 (2020) 103662.
[34] A. Schepelmann, K. Geberth, H. Geyer, Compact nonlinear springs with user defined torque-deflection profiles for series elastic actuators, in: Proceedings - IEEE International Conference on Robotics and Automation, 2014, pp. 3411–3416.
[35] N. Schmit, M. Okada, Synthesis of a non-circular cable spool to realize a nonlinear rotational spring, in: IEEE International Conference on Intelligent Robots and Systems, 2011, pp. 762–767.
[36] H. Bidgoly, M. Ahmadabadi, M. Zakerzadeh, Design and modeling of a compact rotational nonlinear spring, in: IEEE International Conference on Intelligent Robots and Systems, 2016-November, 2016, pp. 4356–4361.
[37] Y.-H. Chen, C.-C. Lan, An adjustable constant-force mechanism for adaptive end-effector operations, Trans. ASME, J. Mech. Des. 134 (3) (2012).
[38] J.-Y. Wang, C.-C. Lan, A constant-force compliant gripper for handling objects of various sizes, Trans. ASME, J. Mech. Des. 136 (7) (2014) http://dx.doi.org/10.1115/1.4027285.
[39] C.-C. Lan, J.-Y. Wang, Design of adjustable constant-force forceps for robot-assisted surgical manipulation, in: Proceedings - IEEE International Conference on Robotics and Automation, 2011, pp. 386–391.
[40] W.W. Van De Sande, A. Ali, G. Radaelli, Design and evaluation of a passive constant force mechanism for a cardiac ablation catheter, J. Med. Dev. 15 (2) (2021) 021003.
[41] X. Zhang, Q. Xu, Design and analysis of a 2-DOF compliant gripper with constant-force flexure mechanism, J. Micro-Bio Robot. 15 (1) (2019) 31–42.
[42] Y. Liu, Z. Li, S. Bai, Design of a reconfigurable novel constant-force mechanism for assistive exoskeletons, in: IFToMM Symposium on Mechanism Design for Robotics, Springer, 2021, pp. 122–131.
[43] B. Ding, J. Zhao, Y. Li, Design of a spatial constant-force end-effector for polishing/deburring operations, Int. J. Adv. Manuf. Technol. 116 (11) (2021) 3507–3515.
[44] P. Wang, Q. Xu, Design and testing of a flexure-based constant-force stage for biological cell micromanipulation, IEEE Trans. Autom. Sci. Eng. (2017) http://dx.doi.org/10.1109/TASE.2017.2733553.
[45] S. Sanchez-Salinas, C. Nunez-Torres, J. Lopez-Martinez, D. Garcia-Vallejo, J.M. Muyor, Design and analysis of a constant-force bench press, Mech. Mach. Theory 142 (2019) 103612.
[46] L. Howell, S. Magleby, Substantially constant-force exercise machine, 2006, US Patent 7,060,012.
[47] D. Smith, Resistive exercise device, 2005, National Aeronautics and Space Administration (NASA), Washington, DC, US Patent 6,958,032.

[48] Y.-H. Chen, C.-C. Lan, Design of a constant-force snap-fit mechanism for minimal mating uncertainty, Mech. Mach. Theory 55 (2012) 34–50.
[49] Z. Li-Jun, L. Tao, S. Bao-Yu, Optimum design of automobile diaphragm spring clutch, in: 2008 IEEE Vehicle Power and Propulsion Conference, VPPC 2008, 2008, pp. 1–4.
[50] B. Weight, C. Mattson, S. Magleby, L. Howell, Configuration selection, modeling, and preliminary testing in support of constant force electrical connectors, Trans. ASME, J. Electron. Packag. 129 (3) (2007) 236–246.
[51] A. Cardona, E. Lens, N. Nigro, Optimal design of cams, Multibody Syst. Dyn. 7 (3) (2002) 285–305, http://dx.doi.org/10.1023/A:1015278213069.
[52] T. Ouyang, P. Wang, H. Huang, N. Zhang, N. Chen, Mathematical modeling and optimization of cam mechanism in delivery system of an offset press, Mech. Mach. Theory 110 (2017) 100–114, http://dx.doi.org/10.1016/j.mechmachtheory.2017.01.004.
[53] L. Xu, A method for modelling contact between circular and non-circular shapes with variable radii of curvature and its application in planar mechanical systems, Multibody Syst. Dyn. 39 (3) (2017) 153–174, http://dx.doi.org/10.1007/s11044-016-9549-0.
[54] A. Borboni, F. Aggogeri, I. Elamvazuthi, G. Incerti, P. Magnani, Effects of profile interpolation in cam mechanisms, Mech. Mach. Theory 144 (2020) http://dx.doi.org/10.1016/j.mechmachtheory.2019.103652.
[55] P. Danakas, M. Bilodeau, N. Quaegebeur, Cam-follower mechanism for airborne ultrasound generation, Appl. Acoust. 182 (2021) http://dx.doi.org/10.1016/j.apacoust.2021.108225.
[56] R. Rayner, M. Sahinkaya, B. Hicks, Improving the design of high speed mechanisms through multi-level kinematic synthesis, dynamic optimization and velocity profiling, Mech. Mach. Theory 118 (2017) 100–114, http://dx.doi.org/10.1016/j.mechmachtheory.2017.07.022.
[57] P. Bergström, O. Edlund, Robust registration of point sets using iteratively reweighted least squares, Comput. Optim. Appl. 58 (3) (2014) 543–561, http://dx.doi.org/10.1007/s10589-014-9643-2.
[58] J. Baumgarte, Stabilization of constraints and integrals of motion in dynamical systems, Comput. Methods Appl. Mech. Engrg. 1 (1) (1972) 1–16, http://dx.doi.org/10.1016/0045-7825(72)90018-7.
[59] D.M. Frost, J.B. Cronin, R.U. Newton, A comparison of the kinematics, kinetics and muscle activity between pneumatic and free weight resistance, Eur. J. Appl. Physiol. 104 (6) (2008) 937–956.
[60] S. Orange, J. Metcalfe, A. Liefeith, P. Marshall, L. Madden, C. Fewster, R. Vince, Validity and reliability of a wearable inertial sensor to measure velocity and power in the back squat and bench press, J. Strength Cond. Res. 33 (9) (2019) 2398–2408, http://dx.doi.org/10.1519/JSC.0000000000002574.